Microstructural Records of Earthquakes in the Lower Crust and Associated Fluid-Driven Metamorphism in Plagioclase-Rich Granulites

Arianne Petley-Ragan, Kristina G. Dunkel, Hakon Austrheim, Benoit Ildefonse, Bjorn Jamtveit

Journal of Geophysical Research: Solid Earth

RESEARCH ARTICLE
10.1029/2017JB015348

Special Section:
Seismic and Micro-Seismic Signature of Fluids in Rocks: Bridging the Scale Gap

Microstructural Records of Earthquakes in the Lower Crust and Associated Fluid-Driven Metamorphism in Plagioclase-Rich Granulites

Arianne Petley-Ragan[1], Kristina G. Dunkel[1], Håkon Austrheim[1], Benoit Ildefonse[2], and Bjørn Jamtveit[1]

[1]Physics of Geological Processes, The Njord Centre, Department of Geosciences, University of Oslo, Oslo, Norway, [2]Géosciences Montpellier, CNRS, University of Montpellier, Université des Antilles, Montpellier, France

Abstract Coseismic damage associated with earthquakes in the lower continental crust is accompanied by postseismic annealing and fluid-mediated metamorphism that influence the physical and chemical development of the continental crust on regional scales. A transition from brittle deformation to crystal-plastic recrystallization is a recurring characteristic of rocks affected by lower crustal earthquakes and is observed in plagioclase adjacent to pseudotachylytes in granulite facies anorthosites from the Bergen Arcs, western Norway. The microstructural and petrological records of this transition were investigated using electron microscopy, electron microprobe analysis, and electron backscatter diffraction analysis. Microfractures associated with mechanical twins are abundant within plagioclase and contain fine-grained aggregates that formed by fragmentation with minor shear deformation. The presence of feather features, which are described for the first time in feldspar, suggests that fractures propagate at near the shear wave velocity into the wall rock of earthquake slip planes. Grain size insensitive recrystallization took place within the time frame of pseudotachylyte formation, forming high-angle grain boundaries required for shear zone initiation. Fluid infiltration synfracture to postfracture facilitated the epitactic replacement of plagioclase by alkali feldspar and the nucleation of clinozoisite, kyanite, and quartz. The grain size reduction and crystallization associated with the microfractures create rheologically weak areas that have the potential to localize strain within the plagioclase-rich lower crust.

Key Points:
- Plagioclase deforms by microfracturing, mechanical twinning, and feather feature formation without major shear component
- Recrystallization of microfractures occurred within the time frame of pseudotachylyte formation
- Microstructures produced by coseismic damage control the spatial distribution of eclogite facies minerals

Supporting Information:
- Supporting Information S1

Correspondence to:
A. Petley-Ragan,
a.j.petley-ragan@geo.uio.no

Citation:
Petley-Ragan, A., Dunkel, K. G., Austrheim, H., Ildefonse, B., & Jamtveit, B. (2018). Microstructural records of earthquakes in the lower crust and associated fluid-driven metamorphism in plagioclase-rich granulites. *Journal of Geophysical Research: Solid Earth*, *123*, 3729–3746. https://doi.org/10.1029/2017JB015348

Received 13 DEC 2017
Accepted 8 MAY 2018
Accepted article online 16 MAY 2018
Published online 30 MAY 2018

1. Introduction

The lower continental crust is mainly composed of feldspar-rich granulites and amphibolites (Rudnick & Fountain, 1995). Many of these rocks are metastable but survive due to the sluggishness of solid-state reactions in the absence of fluids. Earthquakes in the lower crust of continent-continent collision zones open the system to external fluids (Austrheim, 2013; Austrheim et al., 1997; Camacho et al., 2005; Jamtveit et al., 2016), and the fluid-driven retrograde metamorphism that follows (e.g., granulite-eclogite or granulite-amphibolite transitions) leads to localized weakening and associated development of shear zones (Austrheim, 1987; Austrheim & Griffin, 1985; Boundy et al., 1992; Jamtveit et al., 1990; Jolivet et al., 2005; Menegon et al., 2017). Earthquake-triggered metamorphism therefore has important implications for the reworking of the lower crust and the evolution of orogenic belts (Jamtveit et al., 2018).

The wall rocks of middle to lower crustal earthquakes experience extensive damage through fracturing and fragmentation processes before they undergo metamorphic reactions. Petrological studies of exhumed pseudotachylyte-bearing rocks and coseismic loading experiments using electron backscatter diffraction (EBSD) techniques have improved our understanding of the behavior of minerals at conditions imposed by middle to lower crustal earthquakes. These studies describe microfractures containing fragments with crystallographic orientations inherited from their host (Bestmann et al., 2012, 2016; Trepmann et al., 2013), fragmentation without significant shear deformation (Austrheim et al., 2017), and microshear zones of recrystallized grains with random crystallographic orientations (Bestmann et al., 2011, 2012; Mukai et al., 2014; Trepmann et al., 2007). These microstructures are a result of coseismic loading followed by annealing within minutes of seismic slip and have been recorded in quartz, olivine, and garnet. However, few studies address coseismic microstructures in plagioclase feldspar and the fluid-driven metamorphism and rapid crystallization that accompany microfracture annealing in most natural samples.

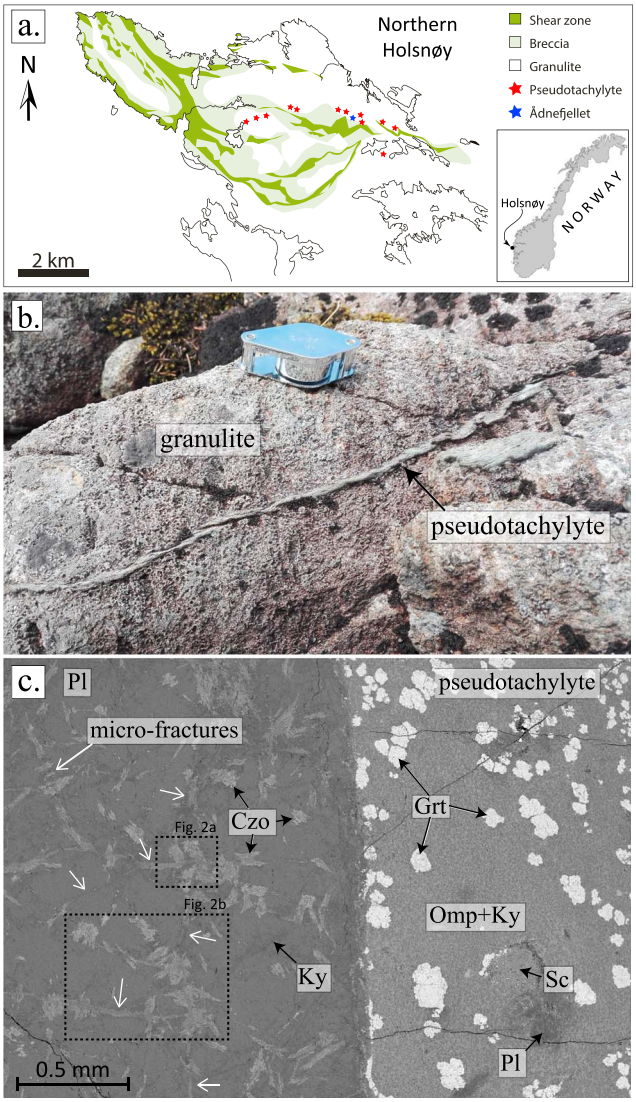

Figure 1. (a) Geological map of Northern Holsnøy modified after Austrheim (2013) with pseudotachylyte localities after Bjørnerud et al. (2002). Sample location: 60°35′32.86″N, 005°04′05.46″E (blue star). The shear zones are made up of eclogite and amphibolite, while the breccia is made of up of eclogite, amphibolite, and granulite. Inset shows the location of Holsnøy Island in western Norway. (b) Field photograph of pseudotachylyte in anorthositic granulite. (c) Backscatter electron image of pseudotachylyte with dendritic garnet (Grt) and clasts of scapolite (Sc) and plagioclase (Pl) in a matrix of omphacite (Omp) and kyanite (Ky) with minor amphibole and Pl. The Pl in the wall rock is riddled with microfractures (indicated by white arrows), clinozoisite (Czo) bundles, and Ky needles. Electron backscatter diffraction analysis was completed on microfractures 1 mm from the pseudotachylyte (Figure 2b). Note that the orientation of the pseudotachylyte is vertical in the sample.

Coseismic microstructures are characterized by significant grain size reduction by brittle mechanisms and/or low-temperature plasticity followed by recrystallization. The formation of fine-grained aggregates by grain size insensitive deformation (i.e., dynamic recrystallization) in plagioclase leads to grain size sensitive deformation mechanisms such as diffusion- and dislocation-accommodated grain boundary sliding under continued deformation (Miranda et al., 2016; Okudaira et al., 2016; Svahnberg & Piazolo, 2010). Grain size sensitive deformation is recognized as a dominant mechanism within lower crustal shear zones. The grain size reduction caused by lower crustal seismicity may therefore contribute to the later development of shear zones near former pseudotachylyte-bearing faults or potentially on the pseudotachylytes themselves (Menegon et al., 2017).

Here we report microstructural developments in plagioclase located in wall rock granulites adjacent to eclogite facies pseudotachylytes from the Bergen Arcs. These rocks are considered analogues to the subducting lower crust beneath Tibet in the present-day Himalayan mountain belt (Austrheim & Boundy, 1994; Jackson et al., 2004). Detailed analysis of the microstructures in plagioclase that experienced lower crustal seismicity may therefore shed valuable light on the response of the feldspar-rich roots of many active orogenic belts. Furthermore, the described microstructures are potentially diagnostic of high-stress deformation at lower crustal conditions.

2. Geological Setting

The Bergen Arcs are a series of arcuate thrust sheets centered on the city of Bergen, western Norway. The investigated pseudotachylyte-bearing rocks are located in the Lindås nappe on the island of Holsnøy where anorthositic rocks are the dominant lithology (Figure 1a) (Austrheim & Griffin, 1985). The Lindås nappe experienced granulite facies metamorphism 930 Ma and was accreted onto the Western Gneiss Region during the Caledonian collision 430–420 Ma (Corfu et al., 2014). Upon collision, the granulites subducted to depths of ~60 km (Boundy et al., 1992) where seismic faults provoked fluid-induced metamorphism to eclogite and amphibolite facies. Pseudotachylyte formation has been recently estimated to have occurred at 680°C and 1.5 GPa (Bhowany et al., 2017). Estimated eclogitization conditions are within 650–750°C and 1.5–2.2 GPa throughout the Bergen Arcs (Bhowany et al., 2017; Boundy et al., 1992; Glodny et al., 2008; Jamtveit et al., 1990), and amphibolization has been inferred to postdate eclogitization and occurs near 600°C and 0.8–1.0 GPa (Glodny et al., 2008).

The exhumed terrane is made up of all three metamorphic facies in a medley of eclogite and amphibolite ductile shear zones, partially metamorphosed breccia (Figure 1a), cataclastic damage zones, and pseudotachylyte-bearing faults (Figure 1b). The damage zones comprise aphanitic pseudotachylyte veins and granulite clasts. The ductile shear zones consist predominantly of eclogite or amphibolite and occasionally recrystallized pseudotachylyte (Austrheim, 2013). The wall rock adjacent to the pseudotachylytes and the clasts in the damage zones are highly fractured and metamorphosed on the micrometer scale (Austrheim et al., 2017) but retain their granulite fabric and mineralogy. Wall rock plagioclase is riddled with a network of microfractures (Figure 1c) that are associated with clinozoisite, kyanite, quartz, alkali feldspar, oligoclase, and labradorite-bytownite in microstructural domains described below. The wall rock damage described in this study is located up to

10 cm from the pseudotachylyte shown in Figure 1c; however, microfractures and associated microstructures are found in all the altered granulite rocks in the Bergen Arcs (Figure S1).

3. Methods

Samples of pseudotachylyte-bearing granulites were collected on Ådnefjellet near the eastern margin of an area subject to extensive shear zone development (Figure 1a).

A Hitachi SU5000 field emission scanning electron microscope and an electron microprobe analyzer Cameca SX100 at the University of Oslo's Department of Geosciences were used for obtaining photomicrographs and quantifying micrometer scale mineral compositions. A beam diameter of 1 μm, an accelerating voltage of 15 kV, and a beam current of 5–10 nA was used for electron microprobe analysis. Further microstructural analysis was done using a CamScan X500FE Crystal Probe equipped with an Oxford/Nordlys EBSD detector at Géosciences Montpellier at the University of Montpellier in France. The EBSD was run with an accelerating voltage of 17 kV, a sample tilt of 70°, a working distance of 25 mm, and a step size of 0.2 μm.

The Matlab toolbox MTEX (version 4.4.0) was used to construct EBSD maps and perform grain analysis (Bachmann et al., 2010; Hielscher & Schaeben, 2008). High-angle grain boundaries are defined by misorientations ≥10° (black in EBSD maps), while low-angle grain boundaries are defined by misorientations <10° (red in EBSD maps). Grains and subgrains <1 μm in diameter (5 pixels) were removed. For the analysis of only small grains and crystals, grains ≥100 μm in diameter (500 pixels) were removed. Contoured pole figures for crystallographic preferred orientations (CPOs) were computed based on one average orientation per grain and are plotted in equal area lower hemisphere plots parallel to the sample reference frame. *J* and *M* indices were calculated in order to quantify the strength of the CPOs (Mainprice et al., 2014). Shape preferred orientations (SPOs) were illustrated in rose diagrams. Maps of the difference between the orientation of individual pixels and the average orientation of the grain they belong to (Mis2Mean) were created for plagioclase in order to illustrate internal strain.

Misorientation axes for plagioclase were analyzed in order to determine the dominant deformation mechanism that created low-angle grain boundaries, tilt-type arrangement of edge dislocations or twist-type arrangement of screw dislocations. In addition to plotting the misorientation axes for low-angle grain boundaries (1–10°), the distribution of all misorientation angles between neighboring and nonneighboring grains (2–178°) was studied as well. Twin misorientations (178–180°) in plagioclase were removed.

A pseudosection was calculated using Perple_X 6.6.8 (Connolly, 2005) with the composition of the wall rock plagioclase in the system Na_2O-CaO-K_2O-Al_2O_3-SiO_2-H_2O. The internally consistent data set of Holland and Powell (Holland & Powell, 1998, updated 2002) was used. Solution models were used for clinopyroxene (Holland & Powell, 1998), mica (Auzanneau et al., 2010; Coggon & Holland, 2002), sanidine (Thompson & Hovis, 1979), and plagioclase (Newton et al., 1980). The activity of H_2O and K_2O was used as independent variables with fixed pressure and temperature of 1.5 GPa and 650°C.

4. Results

4.1. Petrography

The anorthositic granulite facies host rocks are composed of plagioclase (X_{An} = 0.40–0.50), garnet (X_{Pyr} = 0.51, X_{Alm} = 0.30, X_{Grs} = 0.19), Al-rich diopside (X_{Di} = 0.77), S-scapolite (X_{Me} = 0.70), and spinel. Plagioclase is the dominate phase with ~70 vol. %, followed by garnet ~15 vol. % and diopside ~10 vol. %. Scapolite and spinel make up the remaining 5 vol. %. A weak foliation is present as alternating garnet-diopside-scapolite-enriched domains within the plagioclase-dominated volumes. The wall rock plagioclase in Figure 1c has a homogeneous low calcic composition of X_{An} = 0.40. Elongated blebs (<5 μm) of alkali feldspar are found isolated within the interior of plagioclase.

The eclogite facies mineralogy is present within both the pseudotachylyte and the wall rock. The pseudotachylyte in Figure 1c consists of grossular-rich dendritic garnet (X_{Pyr} = 0.30–0.40, X_{Alm} = 0.40–0.46, X_{Grs} = 0.20–0.24) and a matrix mainly composed of fine-grained (grain size 5–20 μm) omphacite (X_{Jd} = 0.18–0.28) and kyanite, and locally clinozoisite spherulites reaching 100 μm in diameter. Minor

amounts of amphibole, sulfides, rutile, carbonate, and corundum are within the pseudotachylyte along with wall rock clasts. The eclogitization of the granulite facies minerals up to at least 1 m from the pseudotachylyte wall is visible on grain boundaries, within microfractures, along cleavage and twin planes, and as inclusions. Spatial heterogeneities are present within single plagioclase grains where microstructural domains located $<$1 mm apart are composed of different eclogitization products.

4.2. Microstructural Domains in Plagioclase

4.2.1. Microfractures

Wall rock plagioclase from Holsnøy displays three types of microfractures based on their mineralogy: (1) feldspar only (Pl + Kfs), (2) quartz-feldspar (Qtz + Pl + Kfs), and (3) kyanite-quartz-feldspar (Ky + Qtz + Pl + Kfs). The microfractures transition between different types over less than a few microns (Figures 2a and 2b). The microfractures described below are from three plagioclase host grains, hereafter referred to as Plagioclase I, II, and III, located 1 mm, 1.5 cm, and 10 cm from the pseudotachylyte in Figure 1c, respectively. The amount of damage by microfractures is high in Plagioclase I (Figure 1c) and decreases toward Plagioclase II and III. These features are furthermore associated with clinozoisite-quartz (Czo + Qtz) and clinozoisite-alkali feldspar (Czo + Kfs) intergrowths.

The Pl + Kfs fractures (5–50 μm) are most abundant. They are dominated by 0.1–5 μm polygonal grains of oligoclase (An_{25-31}) which contain a rim of labradorite-bytownite (An_{65-83}; Figures 2c and 2d). Alkali feldspar is typically located along the margins of the thickest fractures (Figures 2a and 2c) but is sometimes dispersed throughout the fractures (Figure 2e). The second type of microfracture (5–15 μm) contains quartz and feldspar (Qtz + Pl + Kfs in Figures 2a and 2b) and is typically associated with clinozoisite intergrowths (see section 4.2.2). The last type of microfracture is defined by the presence of kyanite (Ky + Qtz + Pl + Kfs in Figures 2a and 2b). These occur as either 1–5 μm single kyanite needles (see section 4.2.3) or as 5–10 μm fractures with kyanite, quartz, labradorite-bytownite, oligoclase, and alkali feldspar (Figures 2e and 2f).

Feldspar compositions are displayed in Figure 3a with chemical maps of a Pl + Kfs fracture in Figures 3c–3e. In proximity to the microfracture, the host plagioclase becomes depleted in Ca (Figure 3c) and enriched in Na (Figure 3d), with K concentrated only within the microfracture (Figure 3e). The alkali feldspar grains within the microfractures are more calcic than expected for typical sanidine values at eclogite facies temperatures. The plagioclase grains within the microfracture are compositionally separated into a sodic and calcic component (Figure 3a), of which the compositional distribution resembles the "complex feldspar" described by Mukai et al. (2014) where calcic compositions form rims around a more sodic core (Figure 2d). However, the Ca-rich domains range almost 20 mol. % from An_{65} to An_{83}.

4.2.2. Clinozoisite Bundles

Clinozoisite is intergrown with quartz and/or alkali feldspar in 10–200 μm bundles (Figures 2a, 2b, and 2e). The bundles are typically oriented normal to the fractures and are always present on both sides of the fractures but never within the fractures. Some clinozoisite bundles appear to be rotated, and some are displaced up to 10 μm across a fracture (lower portion of Figure 2b). However, other clinozoisite bundles show no rotation and no displacement (Figure 2a and upper portion of Figure 2b). Clinozoisite is also observed as isolated needles following cleavage planes or as bundles associated with alkali feldspar in the interior of the host plagioclase grains (Figures 2b and 2f).

4.2.3. Secondary Microfractures

Occasionally, sets of smaller microfractures are observed to branch off a larger primary fracture at a regular angle. The secondary microfractures are most commonly decorated with kyanite needles (Figures 4a, 4c, and 4d), but microfractures of single feldspar grains are also observed (Figure 4b). Up to ~50 secondary fractures branch off from *one side* of a primary fracture. Based on 144 measurements, the secondary microfractures intersect the primary fracture at 52 ± 15° (Figure 4e) and vary in length from 25–600 μm (Figure 4f). Secondary fractures from the same set typically fall within 10–20° of each other but can greatly differ in length. The different angles per set may be due to the measurement of their apparent angle instead of their true angle. The spacing between individual secondary fractures can be 5–60 μm, but within a single set the spacing remains at steady intervals that do not deviate from each other by more than 20 μm. The number of secondary fractures decreases as their length increases (Figure 4a), and the longest secondary fractures become less parallel and begin to curve sometimes intersecting one another away from the primary

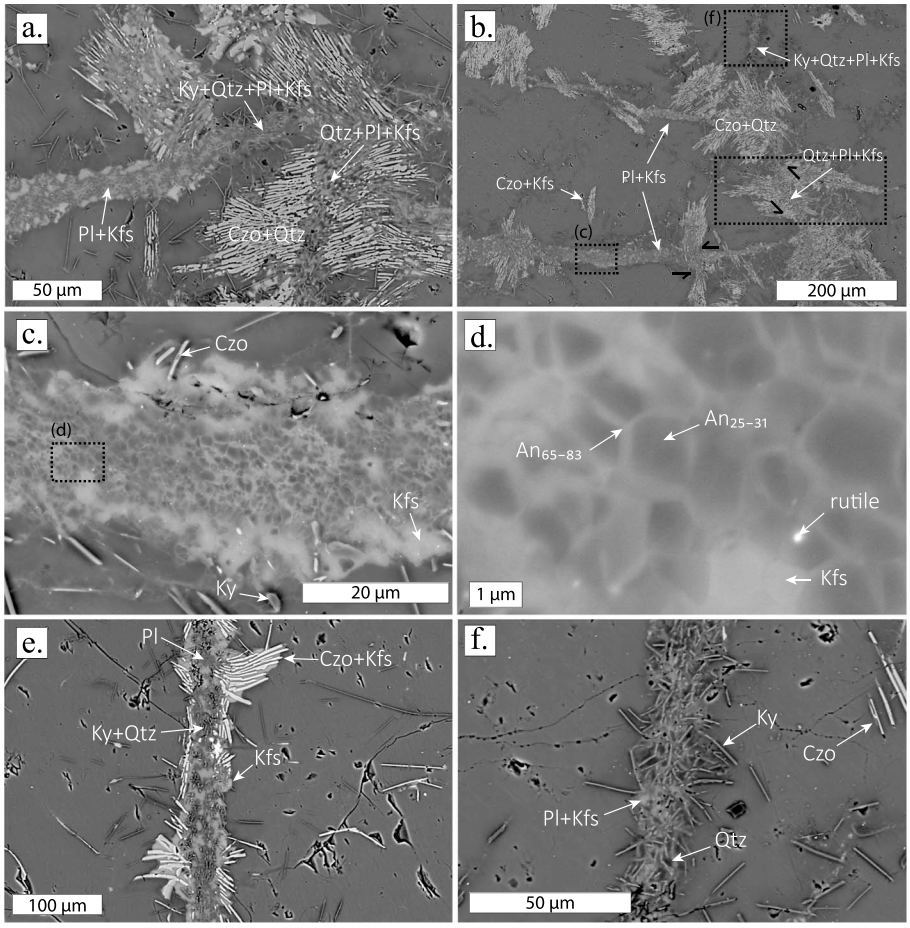

Figure 2. Electron backscatter images of the microstructural domains in Pl from Ådnefjellet. (a) The three types of microfractures: plagioclase-alkali feldspar or feldspar-only (Pl + Kfs), quartz-feldspar (Qtz + Pl + Kfs), and kyanite-quartz-feldspar (Ky + Qtz + Pl + Kfs). The microfractures transition between types over a distance of a few microns. (b) Three microfractures located 1 mm from pseudotachylyte were studied and analyzed with EBSD (black rectangles; see Figure 5). Qtz + Pl + Kfs microfractures are associated with orthogonal Czo bundles that locally show rotation and displacement indicated by the black arrows. (c) Pl + Kfs microfractures contain Kfs, labradorite (light gray), and oligoclase (dark gray). EBSD results are given in Figure 5a. (d) The internal structure of the Pl + Kfs microfractures consists of semipolygonal grains with oligoclase cores and labradorite rims. (e) Ky + Qtz + Pl + Kfs microfracture associated with an orthogonal Czo + Kfs bundle. (f) A Ky + Qtz + Pl + Kfs microfractures with Pl (labradorite and oligoclase) and Qtz. EBSD results are shown in Figure 5b. EBSD = electron backscatter diffraction.

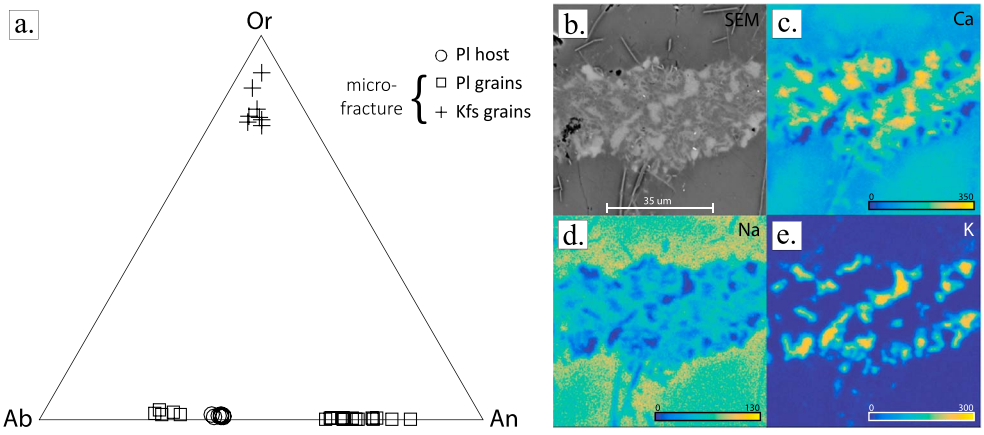

Figure 3. Feldspar compositions. (a) Ternary plot of the composition of the Pl host and the smaller Pl and Kfs grains. (b) Backscatter electron image of Pl + Kfs microfracture analyzed with electron microprobe (c–e). (c) Ca levels in the Pl host decrease toward the microfractures. (d) Na levels in the Pl host increase toward the microfracture. (e) K is concentrated within the microfracture and shows no obvious zoning in the Pl host.

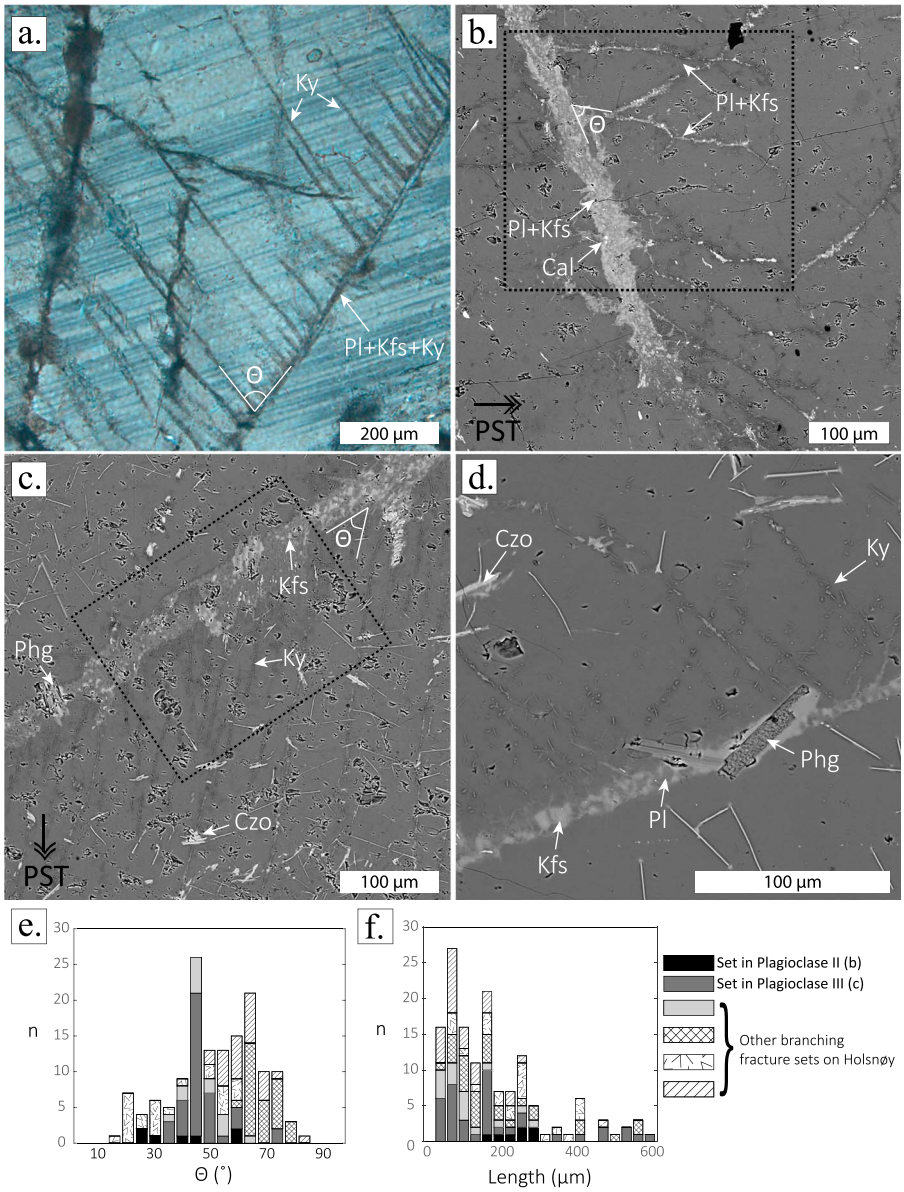

Figure 4. Examples of secondary microfractures in Pl. Black arrows point toward the pseudotachylyte (PST) when known. (a) Cross-polarized microphotograph: a fracture set that branches off from one side of a Ky-dominated microfracture. These fractures are filled by Ky needles. (b) Pl + Kfs secondary fractures on one side of a Pl + Kfs microfracture. Note the presence of calcite (Cal) within the primary microfracture. The indicated area was analyzed with EBSD (Figure 6). (c) Ky needles branch off from a Pl + Kfs microfracture. The indicated area was analyzed with EBSD (Figure 7). (d) Two sets of Ky-filled fractures crosscut each other as they emanate from one side of a Pl + Kfs microfracture in opposite directions. Note the presence of phengite (Phg) within the primary microfracture. (e) Angles measured between branching fractures and the primary microfracture for 144 features. See (a), (b) and (c) for examples of θ. (f) Lengths of the secondary fractures measured from the intersection with the primary microfracture. Measurements were done in Adobe Illustrator. EBSD = electron backscatter diffraction.

fracture. Some primary fractures are observed to contain two sets of secondary fractures emanating in opposite directions and crosscutting each other (Figure 4d), and more rarely some are observed to contain two sets emanating from either side of the same primary fracture. Although present in a number of samples from Holsnøy, these features are not abundant and one thin section may only contain one such set.

4.3. Electron Backscatter Diffraction Results

Three analyzed microfractures from Plagioclase I (one from each type described in section 4.2.1 and shown in Figure 2b) have different orientations relative to the pseudotachylyte wall (90°, 10°, and 30°) and were analyzed with EBSD (Figures 5a–5c). Two additional microfractures with associated secondary fractures were

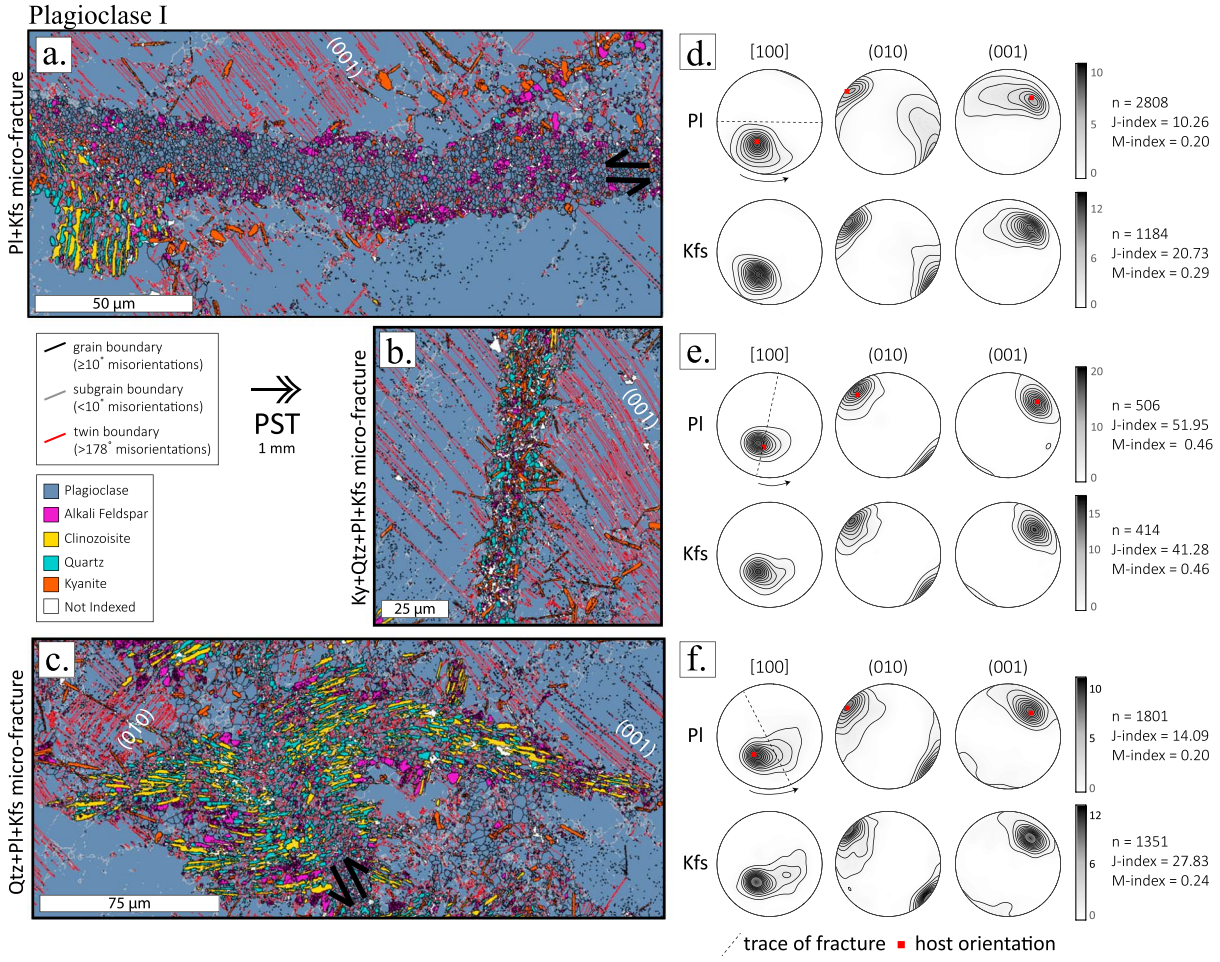

Figure 5. Microstructures and crystallographic orientations from microfractures in Plagioclase I (Figure 2b). Phase maps for (a) Pl + Kfs microfracture (Figure 2c), (b) Ky + Qtz + Pl + Kfs microfracture (Figure 2f), and (c) Qtz + Pl + Kfs microfracture associated with Czo bundle. The spotty appearance of the host Pl is due to small inclusions of other phases. The black arrows on the phase maps indicate the shear direction. The arrow labels PST indicates the direction toward the nearest pseudotachylyte (see Figure 1c). (d–f) Contoured pole figures for Pl and Kfs grains <100 μm in diameter from the EBSD maps shown in (a–c). The orientation distribution functions were computed based on one point per grain and are plotted in equal area lower hemisphere plots, parallel to the sample reference frame. All data are contoured with multiples of 1 of a uniform distribution (MUD). The red squares indicate the average orientation of the host Pl surrounding the microfractures. EBSD = electron backscatter diffraction; PST = pseudotachylyte.

also analyzed (Figures 4b and 4c). The host plagioclase grains in which these two microfractures occur are referred to as Plagioclase II (Figure 6) and Plagioclase III (Figure 7), respectively. The secondary fracture set in Plagioclase II is located 1.5 cm away from a pseudotachylyte (the same as in Figure 1c) with the primary Pl + Kfs fracture oriented ~25° relative to the pseudotachylyte (Figures 4b and 6). The secondary fracture set in Plagioclase III is located about 10 cm from a pseudotachylyte, but the orientation of the primary Pl + Kfs fracture relative to the pseudotachylyte is unknown (Figures 4c and 7). The primary microfractures contain plagioclase grains with a mean area of 1.83 ± 2.22 μm^2 with grain compositions given in Figure 3a and a microstructure similar to the complex feldspar shown in Figure 2d. These grains are defined by high-angle grain boundaries and twin boundaries. Low-angle grain boundaries are abundant within the host plagioclase.

The traces of the primary fractures in Plagioclase I and II do not correspond to any low index crystallographic plane; however, albite and pericline twinning is present in the host (Figures 5a–5c and 6a). The primary fracture within Plagioclase III is the only microfracture whose orientation is parallel to (100), and no twins are present within the host (Figure 7a).

4.3.1. Feldspar Grains Within Microfractures

The CPOs of plagioclase and alkali feldspar grains from all the microfractures inherit the orientation of their host (Figures 5d–5f, 6d, and 7d). However, a slight rotation in the orientation of some feldspar grains has

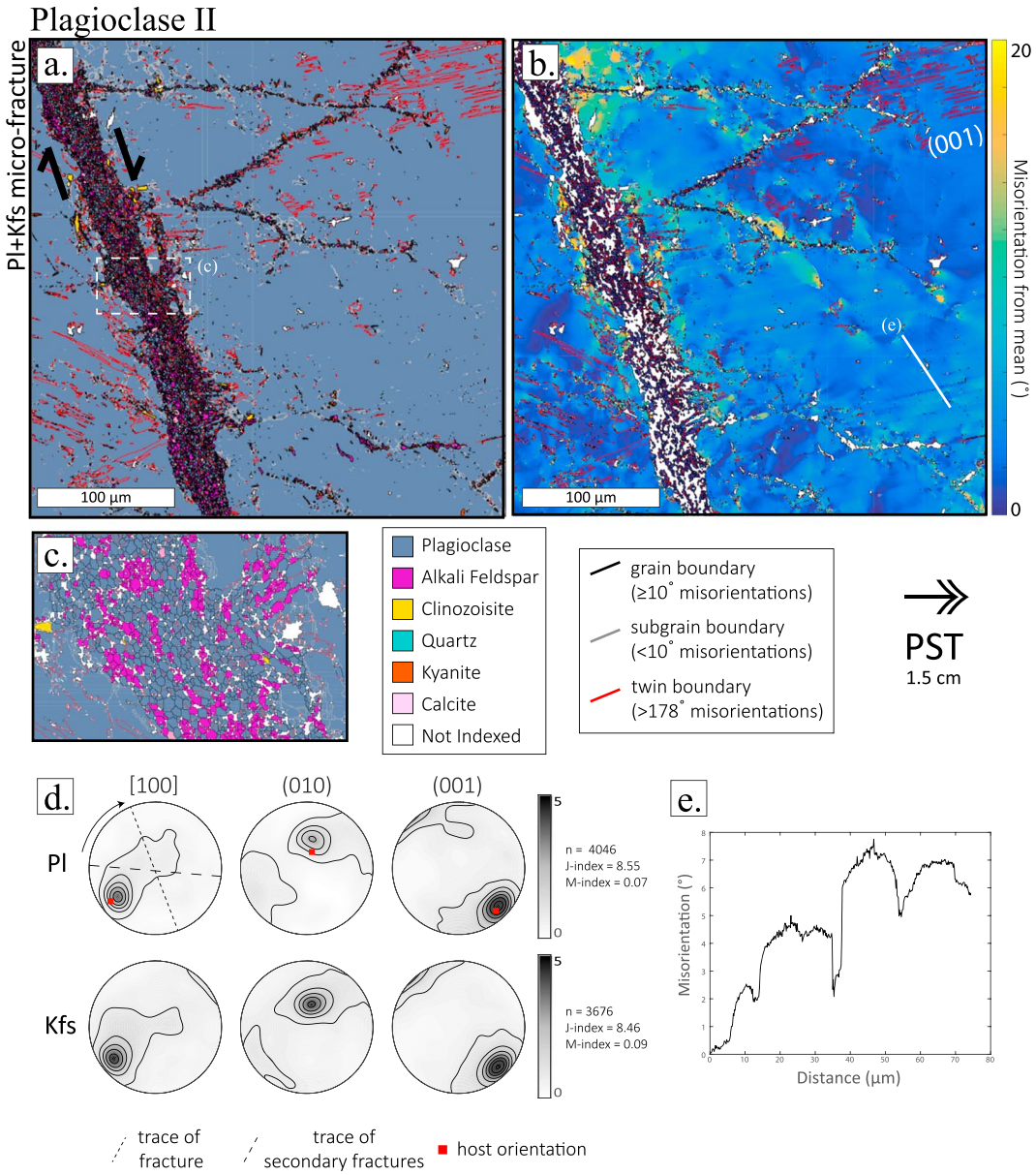

Figure 6. Microstructure, crystallographic orientations, and misorientations from a microfracture with secondary fractures in Plagioclase II (Figure 4b). (a) Phase map showing the primary microfracture on the left (the shear sense is indicated by the black arrows) and several secondary fractures on the right. (b) Internal misorientation map for Pl showing planar features parallel to (001) in the lower right. The misorientation of each point in a grain to the mean orientation of the grain (Mis2Mean) is plotted. White areas are nonindexed points and other phases. The white line gives the position of the misorientation profile shown in (e). (c) Detailed view of the interior of the main microfracture, defined by high-angle grain boundaries between Pl + Kfs. Low-angle grain boundaries are present within the host. The location of this phase map is shown in (a). (d) Slight dispersion and rotation of crystallographic orientations in grains within the fractures, shown in pole figures for Pl and Kfs grains in the microfracture (<100 µm in diameter). The CPO is inherited from the host Pl. The rotation direction coincides with the dextral shear sense of the main fracture, annotated in (a). The CPOs of Pl and Kfs are strongly parallel, suggesting an epitaxial relationship. The orientation distribution functions were computed based on one point per grain and are plotted in equal area lower hemisphere plots in the sample reference frame. Data are contoured with multiples of 1 of a uniform distribution (MUD). (e) Misorientation profile across planar misorientation features seen in (b) that align with Pl(001). The changes in orientation are sharp and 2–4°. CPO = crystallographic preferred orientation; PST = pseudotachylyte.

occurred. The rotation is counterclockwise in the microfractures from Plagioclase I and agrees with the sense of shear illustrated by displaced clinozoisite bundles (see Figures 2b, 5a, and 5c). The rotation of feldspar grains is clockwise in the primary microfracture from Plagioclase II (Figure 6d) and counterclockwise in the primary microfracture from Plagioclase III (Figure 7d). The CPO rotation reflects the sense of shear across these microfractures since other kinematic indicators (i.e., clinozoisite bundles) are absent. *J* and *M* indices,

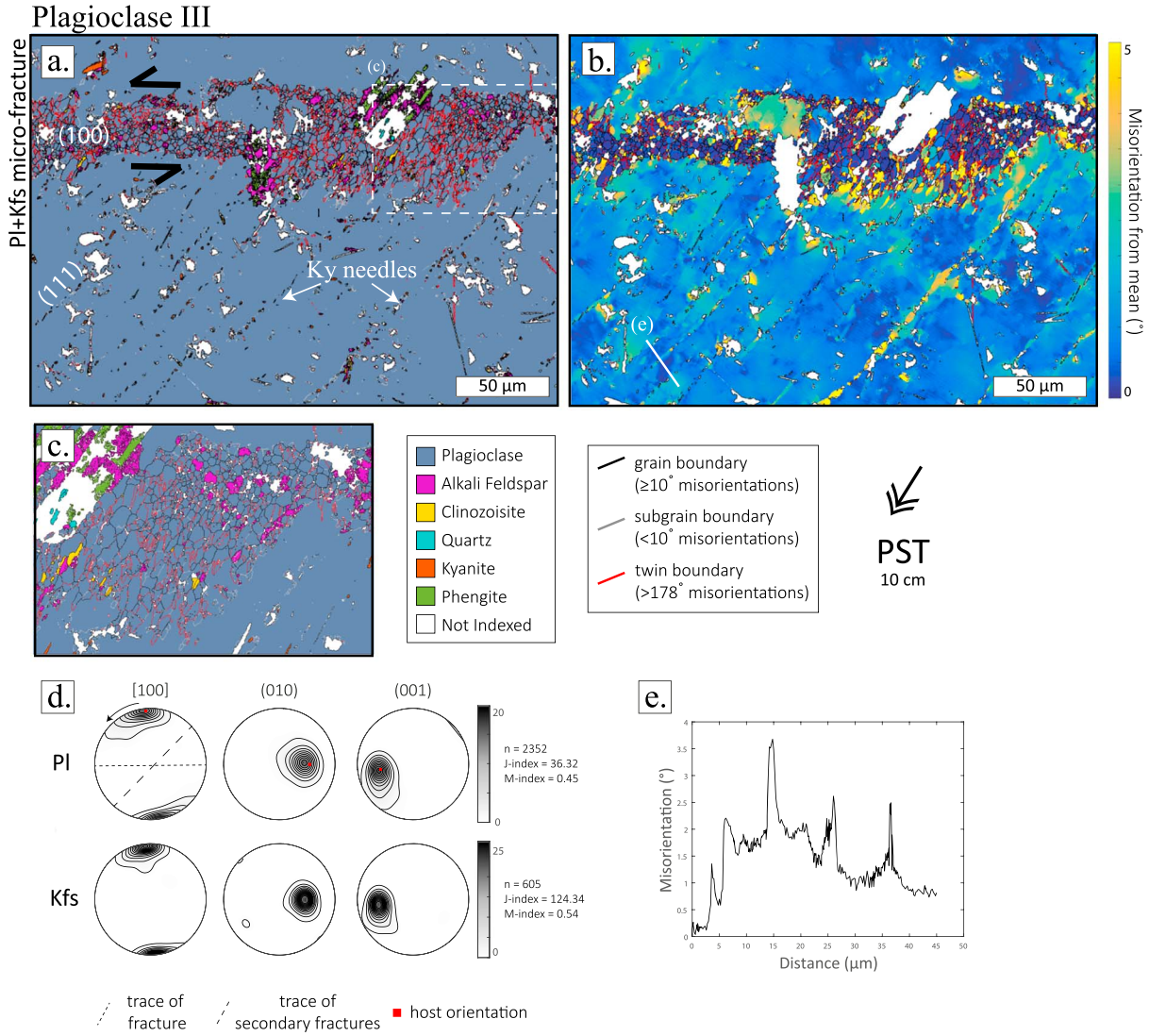

Figure 7. Microstructures, crystallographic orientations, and misorientations from a microfracture with secondary Ky-bearing fractures in Plagioclase III (Figure 4c). (a) Phase map showing a horizontal microfracture (the shear sense is indicated by the black arrows) with diagonal secondary fractures containing Ky needles parallel to (111). The white rectangle denotes the area shown in (c). (b) Internal misorientations, plotted as the misorientation of each pixel from the mean orientation of the respective grain (Mis2Mean) for Pl with white areas as nonindexed points and other phases (i.e., Czo, Kfs, Ky, Phg, and Qtz). Note the coincidence of the changes in misorientation and the location of Ky needles as seen in (a). The white line gives position of the misorientation profile shown in (e). (c) Detailed view of the interior of the primary microfracture showing elongated grains in the bottom left and equant polygonal grains in the top right. (d) Contoured pole figures for Pl and Kfs grains <100 µm in diameter. The orientation distribution functions were computed based on one point per grain and are plotted in equal area lower hemisphere plots parallel to the sample reference frame. Data are contoured with multiples of 2 of a uniform distribution (MUD). (e) Misorientation profile across secondary Ky-bearing fractures in (b) illustrates 5–10 µm intervals of 1–2° planar lattice distortions in the host Pl. PST = pseudotachylyte.

which define the strength of the CPOs, are smallest in the Pl + Kfs microfractures from Plagioclase I (Figure 5d) and II (Figure 6d), both of which show the largest CPO rotation.

A strong SPO is observed in all plagioclase grains within the microfractures (Figure 8). The apparent angle between the orientation of the microfracture and the pseudotachylyte is known within Plagioclase I and II (Figures 8a–8d). Within these fractures, the long axes of the plagioclase grains are approximately parallel to the pseudotachylyte wall in Figure 1c. The skewed SPO distribution for plagioclase from the Qtz + Pl + Kfs fracture (Figure 8c) is a result of plagioclase grains incorporated in the clinozoisite bundle. The angle between the microfracture and the pseudotachylyte is unknown in Plagioclase III, despite of a strong SPO (Figure 8e).

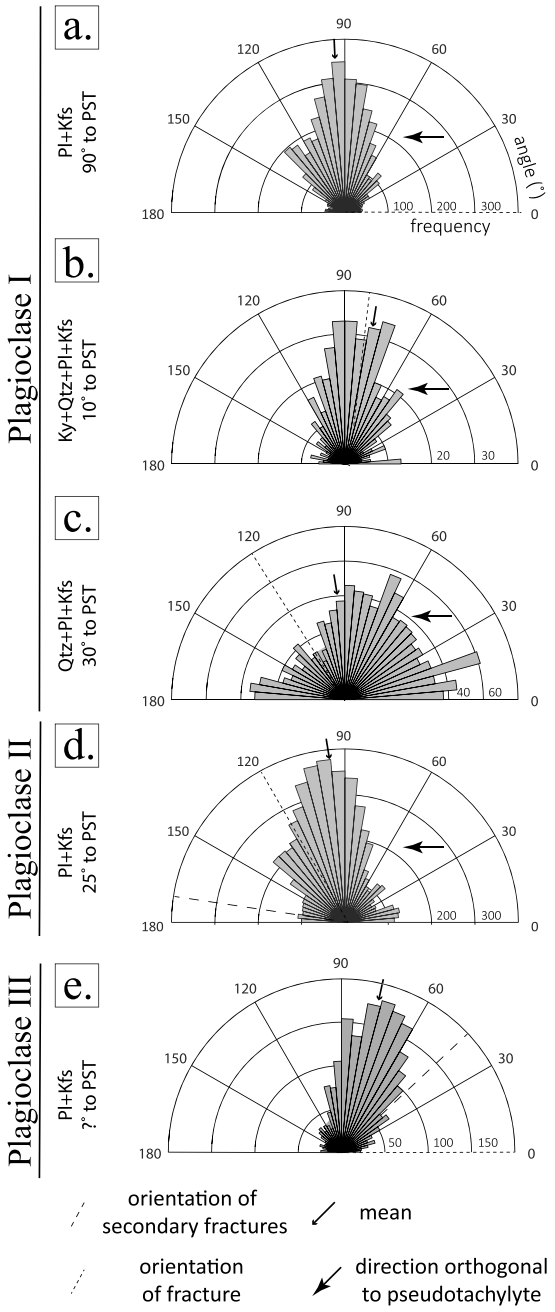

Figure 8. Shape preferred orientations (SPOs) of Pl grains <100 μm in diameter plotted in the sample reference frame. The grain SPOs are compared to the orientation of their corresponding microfracture, the orientation of secondary fractures if present and measureable, and the direction orthogonal to the pseudotachylyte wall. All the Pl grains show a strong SPO unrelated to microfracture orientation. (a) Pl + Kfs microfracture oriented 90° to pseudotachylyte (Figure 5a). (b) Ky + Qtz + Pl + Kfs microfracture oriented 10° to pseudotachylyte (Figure 5b). (c) Qtz + Pl + Kfs microfracture oriented 30° to pseudotachylyte and associated with a Czo bundle (Figure 5c). Note that some of the Pl grains are elongated parallel to the Czo + Qtz bundle (Figure 9), while the mean value remains parallel to pseudotachylyte. (d) Pl + Kfs microfracture oriented 25° to pseudotachylyte from Plagioclase II associated with secondary Pl + Kfs fractures (Figure 6). (e) Pl + Kfs microfracture from Plagioclase III associated with secondary Ky-bearing fractures (Figure 7).

4.3.2. Intracrystalline Deformation Near Secondary Microfractures

Plagioclase II contains secondary microfractures on one side of a Pl + Kfs fracture (Figures 4b and 6). Misorientations of individual pixels from the mean grain orientation (Mis2Mean) are high around the primary and secondary fractures (Figure 6b). The orientation of secondary fractures is not crystallographically related to the host plagioclase. However, planar features parallel to (001) are visible between the secondary fractures and defined by misorientations of 2–6° (Figures 6b and 6e). The misoriented segments are 15–20 μm.

Plagioclase III contains secondary fractures with kyanite needles that extend from one side of a Pl + Kfs fracture (Figures 4c and 7). The internal structure of the primary fracture is similar to the other microfractures with the exception of a portion which contains particularly elongated grains that are defined by a higher number of low angle and twin boundaries compared to the more equant grains which are defined by high-angle grain boundaries (Figure 7c). The elongation of these grains is parallel to the secondary fractures. The secondary fractures are oriented parallel to (111) of the plagioclase host and are associated with small plagioclase misorientations (Figure 7b). A misorientation profile of plagioclase across the fractures shows misorientations of 0.5–2° spaced 10–15 μm apart (Figure 7e).

4.3.3. Clinozoisite-Quartz Bundle

A clinozoisite bundle associated with a Qtz + Pl + Kfs microfracture (Figures 2b and 5c) shows an intimate intergrowth with quartz (Figure 9). Although plagioclase and alkali feldspar grains are present within the intergrowth as well (Figure 5c), clinozoisite and quartz dominate the microstructure. The orientations of individual clinozoisite needles within the bundle do not deviate from each other by more than ~20° (Figure 9a), while individual quartz grains deviate from each other by up to ~80° (Figure 9e). The pole figures suggest no crystallographic relationship between the two phases; however, the poles to (11–20) and (10–10) in quartz lie within the pericline (001) plane of the plagioclase host (Figure 9e). Both clinozoisite and quartz have CPOs with minor clockwise rotation (Figures 9b and 9e) and SPOs that are orthogonal to the orientation of the microfracture (Figures 9c and 9f).

4.3.4. Kyanite Needles

Kyanite in Plagioclase I from the Ky + Qtz + Pl + Kfs microfracture (Figures 2f and 5b) has strong CPOs and SPOs with minor dispersion (Figures 10a and 10b). The SPOs are parallel to the trace of the fracture and would be expected to correspond to the long axis in kyanite, that is, the poles to (001), but instead, they are parallel to the poles to (010). Kyanite in Plagioclase III from the secondary fractures shows CPO and SPO semiparallel to the orientation of the secondary fractures (Figures 10c and 10d) and semiparallel to the SPO in plagioclase from the primary microfracture (see Figure 8e).

4.3.5. Plagioclase Misorientation Analysis

Low-angle misorientation axes and misorientation angle distributions are shown in Figure 11. Since some of the plagioclase host grains contained pericline and albite twins (e.g., Figure 5a), misorientation angles are distributed around both 0° and 180° creating a bimodal distribution of misorientation angles.

The misorientation axes within the Pl + Kfs fractures and the Qtz + Pl + Kfs fracture show maximum near [−100] (Figures 11a, 11e, 11g, and 11i),

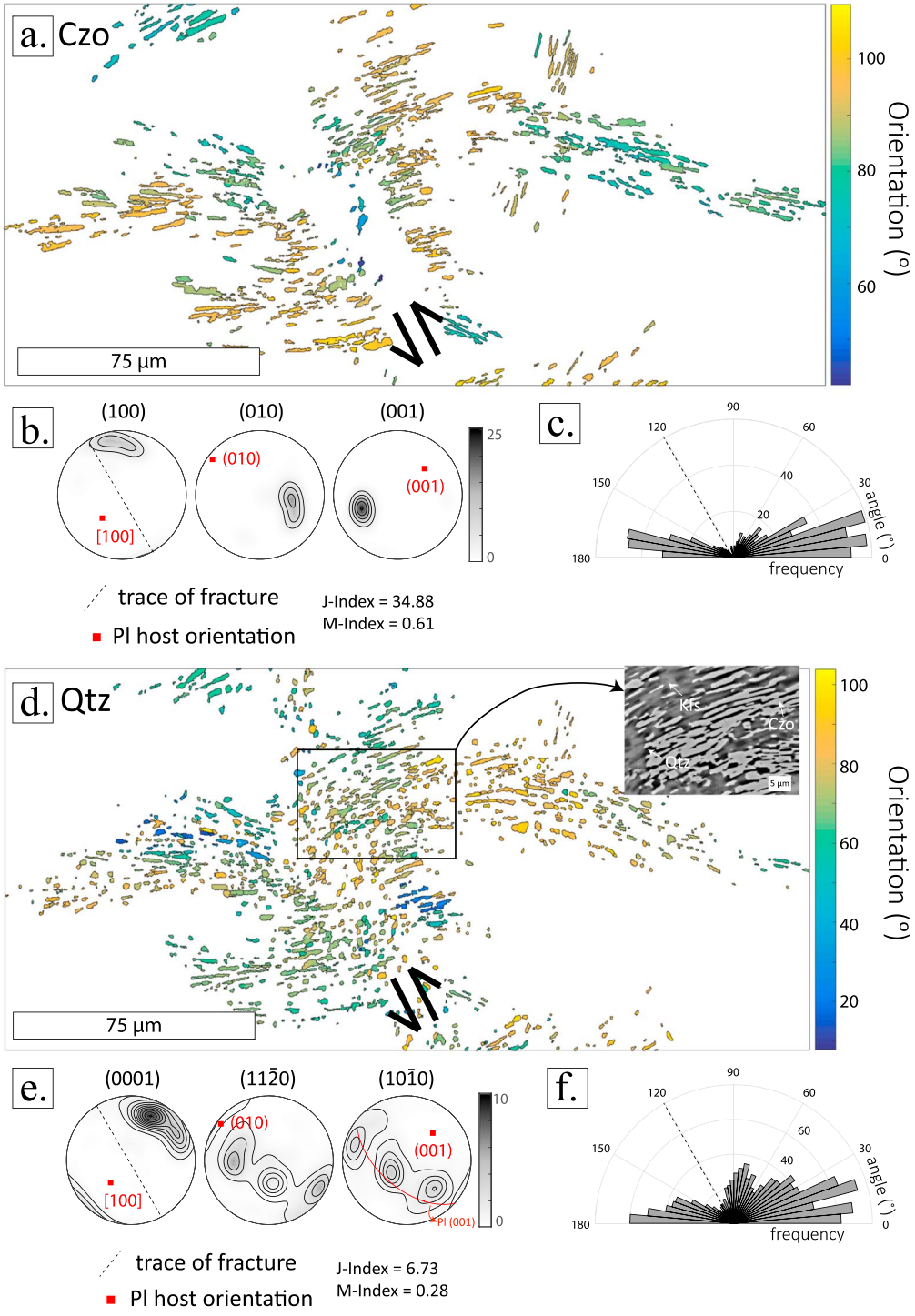

Figure 9. Crystallographic preferred orientations (CPO) and shape preferred orientations (SPO) for a Czo bundle associated with a Qtz-Pl + Kfs microfracture of Plagioclase I (Figure 5c). The bundle also contains Kfs and Pl; however, these do not have as strong a preferred orientation as Czo and Qtz. (a) Orientation of Czo within the bundle in relation to an arbitrary reference point. Note the absence of Czo within the microfracture. (b) Contoured pole figures in equal area lower hemisphere plots for Czo with contour intervals of 5 multiples of uniform distribution (MUD). There is no relation between the orientation of Czo and Pl. (c) The SPO of Czo is orthogonal to the orientation of the microfracture. (d) Orientation of Qtz within the bundle in relation to an arbitrary reference point. Inset shows a backscatter electron image of the microstructure. (e) Contoured pole figures in equal area lower hemisphere plots for Qtz with contour intervals of 1 multiple of uniform distribution (MUD). There is preferences for Qtz to align with Pl(001). (f) The SPO of Qtz is mainly orthogonal to the orientation of the microfracture, similar to that of Czo.

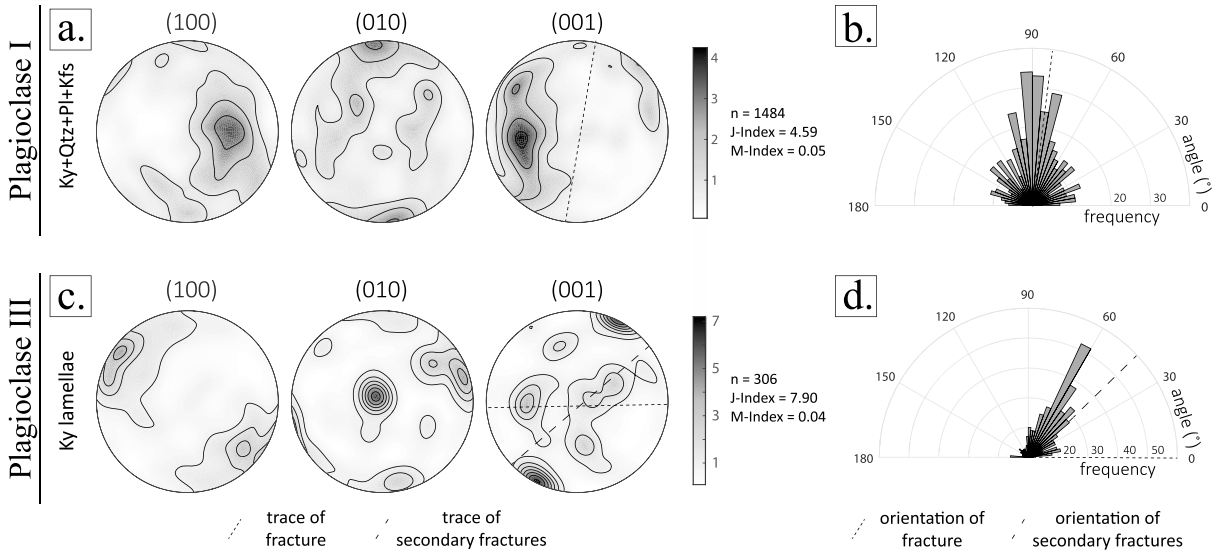

Figure 10. Crystallographic preferred orientations (CPO) and shape preferred orientations (SPO) for Ky in (a, b), the Ky-Qtz-Pl + Kfs microfracture from Plagioclase I (Figure 5b), and (c, d) the secondary fractures of the Pl + Kfs microfracture in Plagioclase III (Figure 7). (a) Contoured pole figures of Ky, plotted in equal area lower hemisphere with contour intervals of 1 multiple of uniform distribution (MUD), show (010) parallel to microfracture orientation. (b) SPO of Ky shows a dispersed orientation subparallel to the microfracture orientation. (c) Contoured pole figures of Ky show (001) semiparallel to the secondary fractures. Plotted in equal area lower hemisphere with contour intervals of 1 multiple of uniform distribution (MUD). (d) SPO of Ky shows an orientation semiparallel to the secondary fractures and semiparallel to the Pl SPO from the same microfracture (Figure 8e).

which corresponds to the production of edge dislocations within the (010)[001] slip system. The Ky + Qtz + Pl + Kfs fracture shows a maximum of misorientation axes at [010] (Figure 11c), which corresponds to screw dislocations associated with the (010)[001] slip system. The two primary fractures in Plagioclase II and III show dispersed misorientation axes between [101] and [201] (Figures 11g and 11i), which represent grain rotation (Miranda et al., 2016). For Plagioclase II, grain rotation is also recorded by its near-random distribution of misorientation angles between neighboring and nonneighboring grain pairs (Figure 11h), whereas the primary fracture in Plagioclase III only contains misorientations up to 40° (from 0° to 180°), indicating subgrain rotation (Kruse et al., 2001; Miranda et al., 2016; Savhnberg & Piazolo, 2010). Subgrain rotation is also responsible for the neighboring and nonneighboring distributions in the other microfractures (Figures 11b, 11d, and 11f). The Pl + Kfs fracture in Plagioclase I has even more high-angle grain boundaries and a nonneighboring distribution approaching random (Figure 11b).

4.4. Thermodynamic Equilibria

A log-log pseudosection of the activity of K_2O (aK_2O) and H_2O (aH_2O) illustrates the effect these species have on the mineral assemblage at eclogite facies conditions based on the bulk composition of plagioclase from Plagioclase I (Figure 12). The choice of K_2O as a component is arbitrary, and so the values on the vertical axis are also arbitrary. Still, the diagram is useful giving relative stability fields of the relevant minerals. Kyanite is associated with all of the studied microfractures limiting the conditions of formation to the region shaded in gray. The majority of the microfractures can be placed into either the Kfs-bearing or Qtz-bearing fields reflecting the strong dependence of the observed mineralogy on the chemical potential of K_2O. The absence of white mica in Plagioclase I and II limits the H_2O activity to $0.03 < aH_2O < 0.20$ in the presence of plagioclase, zoisite, kyanite and quartz or alkali feldspar. The presence of white mica in Plagioclase III indicates $aH_2O > 0.20$.

5. Discussion

Petrological observations and detailed EBSD analysis show that the original granulite facies plagioclase feldspar responds to lower crustal earthquakes by (1) microfracturing, (2) mechanical twinning, (3) secondary fracturing related to low index crystallographic planes, and (4) dynamic recrystallization within the microfractures. The spatial association between eclogite facies minerals and microfractures demonstrates that the

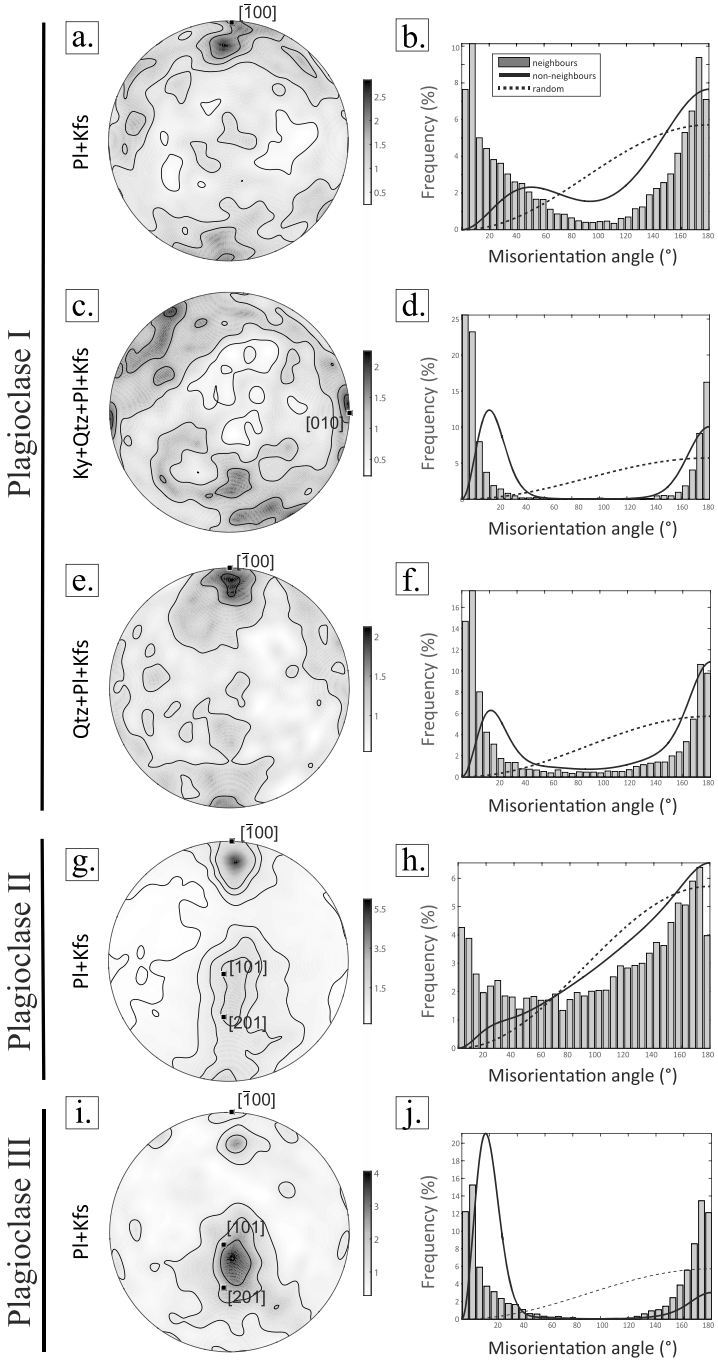

Figure 11. Low-angle misorientation axes distribution and misorientation distributions for the (a, b) Pl + Kfs microfracture (Figure 5a), (c, d) Ky + Qtz + Pl + Kfs microfracture (Figure 5b), (e, f) Qtz-Pl + Kfs microfracture (Figure 5c), (g, h) Pl + Kfs microfracture with secondary fractures (Figure 6), and (i, j) Pl + Kfs microfracture with secondary Ky-bearing fractures (Figure 7). Misorientation axes distributions with maxima at [100] indicate edge dislocations related to (010)[001] and are present in (a, e, g, and i) the Pl + Kfs and Qtz + Pl + Kfs microfractures. Misorientation axes distributions with maxima at [010] indicate screw dislocations related to (010)[001] and are present in (b) the Ky + Qtz + Pl + Kfs microfracture. Misorientation axes distributions with dispersed maxima between [101] and [201] along (010) indicate that grain rotation was present within (g, i) the microfractures associated with secondary fractures. All contours are plotted in intervals of 0.5 multiples of uniform distribution (MUD). Low- and high-angle misorientations between neighboring (bars) and nonneighboring (solid line) grain pairs are plotted compared to a random distribution of misorientations (dotted line). Twin boundaries 178–180° were removed from the analysis; however, misorientations produced from twins are evident from the bimodal distributions of neighbors. Misorientations 2–40° and 140–180° indicate subgrain rotation (b, d, f, and j), and misorientations >40° indicate grain rotation (b, h).

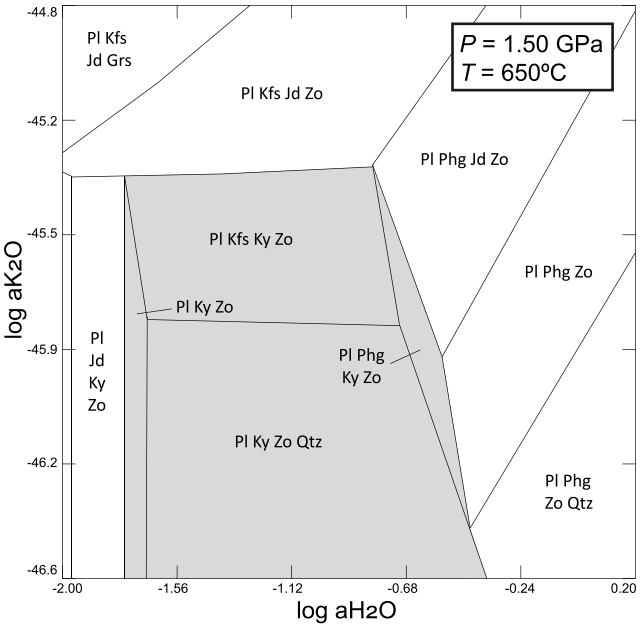

Figure 12. Pseudosection of aH_2O versus aK_2O at 1.5 GPa and 650 °C in the system Na_2O-CaO-K_2O-Al_2O_3-SiO_2-H_2O. K_2O is chosen as an arbitrary component reflecting the chemical potential of potassium in the system. The absolute values for aK_2O are not meaningful, but the arrangement of relative stability fields is valid. The composition used in weight percentages of oxides is as follows: Na_2O = 6.76, Al_2O_3 = 26.35, SiO_2 = 56.86, and CaO = 8.61 (wt. %). The shaded area includes all Ky-bearing assemblages which is representative of the conditions of formation for the studied microfractures. Mineral abbreviations are Grs = grossular, Jd = jadeite, Kfs = alkali feldspar, Ky = kyanite, Phg = phengite, Pl = plagioclase, Qtz = quartz, and Zo = zoisite. Most of the microfractures lie in the Kfs- and Qtz-bearing fields, with the secondary Ky-bearing fractures at the lowest aH_2O values and Phg-bearing microfractures at the highest aH_2O values.

microfractures acted as pathways for fluids to enter into the wall rock and lead to (5) the partial replacement of plagioclase by eclogite facies minerals within and adjacent to the microfractures.

5.1. Coseismic Deformation

We interpret the microfractures in plagioclase as annealed brittle fractures owing to their orientation independent of the host plagioclase crystallography and the inheritance of grain CPOs from the host plagioclase (Figures 5d–5f, 6d, and 7d; Bestmann et al., 2012, 2016; Trepmann et al., 2007). The lack of significant displacement across the fractures and the overall preservation of the shape of the host grain suggest fracturing without a major shear component. The microfracture from Plagioclase II displays grain rotation (Figure 11h), which may, however, be a result of minor cataclastic flow during fracture formation. Fragmentation without significant shear strain, often referred to as pulverization when occurring in less confined near-surface environments (Mitchell et al., 2011; Sullivan & Peterman, 2017), has previously been observed in garnets cut by pseudotachylyte from the same area at Holsnøy (Austrheim et al., 2017).

Along with microfractures, albite and pericline twins are present in Plagioclase I and II (Figures 5a–5c and 6a). The abundance of twin boundaries within the microfractures, even when twins are absent in the host (e.g., Plagioclase III, Figure 7a), and the formation of predeveloped twins between secondary microfractures (e.g., Plagioclase II, Figure 6b) suggest synchronous formation. Bimodal distributions of misorientation angles further support synchronous fracturing and twinning, again even when twins are absent in the host (e.g., Plagioclase III, Figure 11j). In addition, the wedged and sometimes curved shape of the twins and their discontinuity through the host plagioclase implies that the twins are not growth features. Instead, these characteristics are typical of mechanical twins which form under high differential stress. Such features have previously been recognized as diagnostic of shocked feldspar from meteorite impacts (Huffman et al., 1993; Pickersgill et al., 2015; White, 1993). Although some of the twins may be a remnant microstructure from granulite facies metamorphism, the discontinuity of most twins across the microfractures (e.g., Plagioclase I, Figure 5a) suggests that some twins were not present prior to microfracture formation and formed as a result of the high differential stresses imposed by seismic faulting. Slip within the plagioclase structure is preferred along crystallographic planes, but when regional stresses are not oriented to accommodate slip along twin planes (i.e., "hard" orientations), the formation of fractures may act to reorient the local stresses and aid the formation of mechanical twins (Marshall & McLaren, 1977).

The planar features represented by secondary microfractures in the host Plagioclase III are unrelated to common crystallographic twin planes (Figure 7). These features are parallel to the low index crystallographic plane (111) and decorated with kyanite. They resemble so-called *feather features* which have been interpreted as diagnostic of low shock metamorphism (7–10 GPa) in quartz (French & Koeberl, 2010; French et al., 2004; Poelchau & Kenkmann, 2011; Zaag et al., 2016). The measured angles between the secondary fractures and the primary fractures (Figure 4e) are consistent with the average angle of feather features (57 ± 11°) as found by Poelchau and Kenkmann (2011). Furthermore, based on experimental results, feather features occur on the side of a planar fracture from which the shock wave came and their acute angle points in the opposite direction of shear along the planar fracture (Poelchau & Kenkmann, 2011). Nearly all secondary fractures observed point in the direction of the nearest pseudotachylyte. However, from the two secondary fractures analyzed, only the kyanite-bearing fractures in Plagioclase III contain an acute angle that points in the opposite direction of the sense of rotation of grain CPOs in the primary fracture (Figures 7a and 7d). The secondary fractures in Plagioclase II have an acute angle that opens up in the direction of shear along the primary fracture (Figures 6a and 6d). Therefore, we suggest that the kyanite-bearing fractures in Plagioclase III are true

feather features and the branching microfractures in Plagioclase II are secondary fractures that have reoriented local stresses to accommodate slip along (001) twins (Marshall & McLaren, 1977).

The secondary microfractures also resemble tensile microcracks that occur on one side of dynamic shear ruptures that propagate near the shear wave velocities (Griffith et al., 2009). The microfractures with secondary fractures most likely propagated at near the shear wave velocity of granulite (3–4 km/s), creating high stresses in their immediate vicinity that opened tensile cracks or feather features. Therefore, not only did the rupturing associated with pseudotachylyte-bearing faults in the lower crust propagate at near seismic velocities but the microfractures produced coseismically in the wall rock also traveled at comparable speeds.

5.2. Coseismic Annealing

The recrystallization of plagioclase within the microfractures took place through grain size insensitive deformation, forming grains with sharp triple junctions (Figure 2d) and rotations of up to 40° (Figures 11b, 11d, 11f, and 11j). These are characteristics of subgrain rotation (Kruse et al., 2001; Menegon et al., 2017; Miranda et al., 2016; Svahnberg & Piazolo, 2010; Trepmann et al., 2007). The low-angle grain boundaries formed by mostly tilting and sometimes twisting of dislocations related to the (010)[001] slip system (Figures 11a, 11c, 11e, 11g, and 11i). The (010)[001] slip system is responsible for the observed albite twinning and illustrates the importance of mechanical twins in the development of grain boundaries during recrystallization within the microfractures. The presence of subgrains, and sometimes grains, within the host plagioclase which are of the same order of magnitude in size as the grains within the microfractures (i.e., lower right of Figure 5c) suggests that recrystallization by subgrain rotation was also active in the host.

Variably sized fragments with a high density of defects were most likely present within the fractures immediately after seismic loading, similar to the situation for plagioclase fractures described elsewhere (e.g., Marshall & McLaren, 1977; Stünitz et al., 2003). Grain size reduction of large fragments through dynamic recrystallization (Kruse et al., 2001) and growth of smaller fragments acting as nuclei (Trepmann et al., 2013) led to a relatively uniform distribution of plagioclase grain sizes within the microfractures. The strong SPOs indicate that recrystallization took place under stress, and the parallel relationship of SPOs to the pseudotachylyte from microfractures in Plagioclase I and II is evidence that recrystallization was simultaneous to pseudotachylyte formation (Figures 8a–8d). Grain SPOs orthogonal to the principle stress direction are observed in dynamically recrystallized plagioclase and quartz under stress (Svahnberg & Piazolo, 2010; Trepmann et al., 2007). This chronologically places the annealing of the microfractures within the time frame of seismic slip. According to a transient thermal model by Bestmann et al. (2012), annealing of quartz microfractures takes place within seconds for tonalitic wall rock located ~2 cm from a 1.5-cm-thick frictional melt vein. After ~5 min, the conditions have returned to ambient temperature, which in their case is ~300°C, much lower than the eclogite facies conditions in the Bergen Arcs (650–750°C).

The distribution of Ca within the microfractures creating oligoclase and labradorite-bytownite domains is spatially associated with the fabric of the plagioclase grains, creating a Ca-rich "network" that follows the grain boundaries (Figures 2d and 3c), suggesting that it may be a result of recrystallization. However, enrichment of Ca in the rims of dynamically recrystallized plagioclase grains has never been observed to exceed ~6 mol. % (Bestmann et al., 2012; Kruse et al., 2001; Miranda et al., 2016; Okudaira et al., 2016; Svahnberg & Piazolo, 2010). Additionally, dynamic recrystallization by definition should not involve a major change in chemical composition since it is driven by internal strain energy produced by crystal defects (Poirier & Guillope, 1979). Solid-state diffusion of NaSi-CaAl in plagioclase is too slow, even at high temperatures, to explain the observed 20–40 mol. % compositional change within minutes of seismic slip. Furthermore, equilibrium thermodynamics predicts Na enrichment in plagioclase at high pressures with Ca-rich plagioclase becoming unstable around 0.8 GPa (Wain et al., 2001; Wayte et al., 1989). Mukai et al. (2014) attributed the compositional change in what they call the complex feldspar to fluid- and stress-assisted coarsening of Bøggild-type intergrowth.

The formation of fine-grained aggregates promotes grain size sensitive deformation mechanisms (Bestmann et al., 2011, 2012; Miranda et al., 2016; Okudaira et al., 2016; Svahnberg & Piazolo, 2010). However, we conclude that grain size sensitive deformation (i.e., grain boundary sliding) was not yet a dominant deformation mechanism within the microfractures due to the presence of undisplaced clinozoisite bundles (Figure 2a) and kyanite (Figure 2f) and the strong preservation of host-controlled CPOs (Figures 5d–5f, 6d, and 7d). The lack of

postfracture shearing further supports the return to ambient conditions and annealing of microstructures relatively quickly after coseismic fragmentation.

5.3. Seismically Induced Fluid-Driven Metamorphism

During pseudotachylyte formation, the granulite facies mineral assemblage was metastable (Jamtveit et al., 1990). The transformation of the plagioclase-rich granulite to eclogite facies mineralogy is clearly associated with the introduction of fluids. The strong spatial dependence of the microfracture mineralogy (Figure 2a) may reflect subtle variations in fluid composition, in particular, variations in the activity of H_2O and K_2O, as shown in Figure 12. The activity of H_2O may have varied from ~0.02 in the secondary microfractures containing kyanite needles to $\geq$0.20 in the rare phengite-bearing primary microfractures (e.g., Plagioclase III). The spatial differences in microfracture mineralogy probably reflect that the relative rates of fluid transport and fluid-rock interaction vary among the fracture types.

The epitactic replacement of plagioclase grains by alkali feldspar, as shown by parallel CPOs (Figures 5d–5f, 6d, and 7d), required fluid-assisted dissolution precipitation processes (Putnis & Austrheim, 2010). The distribution of alkali feldspar on plagioclase grains, clinozoisite along the edges of the microfractures (Figure 9a), and quartz on plagioclase twins (Figure 9e) indicates that coseismic deformation has significant effects on the distribution of eclogite facies phases. Furthermore, local stresses within the microfractures may have influenced these phases to grow in the direction of the local minimum principle stress creating an orthogonal relationship to their corresponding microfracture (Figures 9c and 9f). At a certain distance from the fractures, the stress-controlled growth is lost, possibly owing to the rotated appearance of some of the clinozoisite bundles (Figure 2b).

Local displacement of clinozoisite bundles (Figure 2b) suggests that fluid-driven metamorphism was simultaneous to fracturing. The coeval nature of fracturing and fluid infiltration may indicate that fracture propagation was driven by the influx of fluid into the wall rock (i.e., hydrofractures). Undisplaced clinozoisite bundles (Figure 2a) and the overgrowth of microfractures by kyanite (Figure 2f) indicate that fluid-driven metamorphism also played a role during fracture annealing.

6. Conclusion

The microstructural response of plagioclase to lower crustal seismicity entails brittle fragmentation in the form of planar fractures with minor shear component, feather feature formation around dynamic ruptures propagating at near the shear wave velocity, dynamic recrystallization within the time frame of seismic slip, and fluid-driven metamorphism synfracture to postfracture formation. The creation of fine-grained aggregates through grain size reduction and dynamic recrystallization, coupled with new phase growth, is a potential trigger for the grain size sensitive mechanisms involved in subsequent shear zone development.

Acknowledgments
This project has been supported by the European Research Council (ERC) Advanced Grant Agreement 669972, "Disequilibrium Metamorphism" ("DIME") to B. J., and the Natural Science and Engineering Research Council (NSERC) of Canada Postgraduate Scholarship Doctoral (PGS-D) 489392 to A. P. R. We thank C. Nevado and D. Delmas for high-quality thin section polishing, F. Barou for assistance with EBSD measurements, and M. Erambert for help on the electron microprobe. We also thank N. Mancktelow for a constructive review. The data are available on Open Science Framework at osf.io/8nm9v.

References

Austrheim, H. (1987). Eclogitization of lower crustal granulites by fluid migration through shear zones. *Earth and Planetary Science Letters*, *81*, 221–232. https://doi.org/10.1016/0012-821X(87)90158%E2%80%930

Austrheim, H. (2013). Fluid and deformation induced metamorphic processes around Moho beneath continent collision zones: Examples from the exposed root zone of the Caledonian mountain belt, W-Norway. *Tectonophysics*, *609*, 620–635. https://doi.org/10.1016/j.tecto.2013.08.030

Austrheim, H., & Boundy, T. M. (1994). Pseudotachylytes generated during seismic faulting and eclogitization of the deep crust. *Science*, *265*(5168), 82–83. https://doi.org/10.1126/science.265.5168.82

Austrheim, H., Dunkel, K. G., Plümper, O., Ildefonse, B., Liu, Y., & Jamtveit, B. (2017). Fragmentation of wall rock garnets during deep crustal earthquakes. *Science Advances*, *3*, 1–8.

Austrheim, H., Erambert, M., & Engvik, A. K. (1997). Processing of crust in the root of the Caledonian continental collision zone: The role of eclogitzation. *Tectonophysics*, *273*(1-2), 129–153. https://doi.org/10.1016/S0040-1951(96)00291-0

Austrheim, H., & Griffin, W. L. (1985). Shear deformation and eclogite formation within granulite-facies anorthosites of the Bergen Arcs, Western Norway. *Chemical Geology*, *50*(1-3), 267–281. https://doi.org/10.1016/0009-2541(85)90124-X

Auzanneau, E., Schmidt, M. W., Vielzeuf, D., & Connolly, J. A. D. (2010). Titanium in phengite: A geobarometer for high temperature eclogites. *Contributions to Mineralogy and Petrology*, *159*(1), 1–24. https://doi.org/10.1007/s00410-009-0412-7

Bachmann, F., Hielscher, R., & Schaeben, H. (2010). Texture analysis with MTEX—Free and open source software toolbox. *Solid State Phenomena*, *160*, 63–68. https://doi.org/10.4028/www.scientific.net/SSP.160.63

Bestmann, M., Pennacchioni, G., Frank, G., Goken, M., & de Wall, H. (2011). Pseudotachylyte in muscovite-bearing quartzite: Coseismic friction-induced melting and plastic deformation of quartz. *Journal of Structural Geology*, *33*(2), 169–186. https://doi.org/10.1016/j.jsg.2010.10.009

Bestmann, M., Pennacchioni, G., Mostefaoui, S., Göken, M., & de Wall, H. (2016). Instantaneous healing of micro-fractures during coseismic slip: Evidence from microstructure and Ti in quartz geochemistry within an exhumed pseudotachylyte-bearing fault in tonalite. *Lithos*, *254-255*, 84–93. https://doi.org/10.1016/j.lithos.2016.03.011

Bestmann, M., Pennacchioni, G., Nielsen, S., Göken, M., & de Wall, H. (2012). Deformation and ultrafine dynamic recrystallization of quartz in pseudotachylyte-bearing brittle faults: A matter of a few seconds. *Journal of Structural Geology*, *38*, 21–38. https://doi.org/10.1016/j.jsg.2011.10.001

Bhowany, K., Hand, M., Clark, C., Kelsey, D. E., Reddy, S. M., Pearce, M. A., et al. (2017). Phase equilibria modelling constraints on P-T conditions during fluid catalysed conversion of granulite to eclogite in the Bergen Arcs, Norway. *Journal of Metamorphic Geology*, *36*(3), 315–342. https://doi.org/10.1111/jmg.12294

Bjørnerud, M., Austrheim, H., & Lund, M. (2002). Processes leading to eclogitization (densification) of subducted and tectonically buried crust. *Journal of Geophysical Research*, *107*(B10), 2252. https://doi.org/10.1029/2001JB000527

Boundy, T. M., Fountain, D. M., & Austrheim, H. (1992). Structural development and petrofabrics of eclogite facies shear zones, Bergen Arcs, western Norway: Implications for deep crustal deformational processes. *Journal of Metamorphic Geology*, *10*(2), 127–146. https://doi.org/10.1111/j.1525-1314.1992.tb00075.x

Camacho, A., Lee, J. K. W., Hensen, B. J., & Braun, J. (2005). Short-lived orogenic cycles and the eclogization of cold crust by spasmodic hot fluids. *Nature*, *435*(7046), 1191–1196. https://doi.org/10.1038/nature03643

Coggon, R., & Holland, T. J. B. (2002). Mixing properties of phengitic micas and revised garnet-phengite thermobarometers. *Journal of Metamorphic Geology*, *20*(7), 683–696. https://doi.org/10.1046/j.1525-1314.2002.00395.x

Connolly, J. A. D. (2005). Computation of phase equilibria by linear programming: A tool for geodynamic modeling and its application to subduction zone decarbonation. *Earth and Planteary Science Letters*, *236*(1-2), 524–541. https://doi.org/10.1016/j.epsl.2005.04.033

Corfu, F., Andersen, T. B., & Gasser, D. (2014). The Scandinavian Caledonides: Main features, conceptual advances and critical questions. *Geological Society, London, Special Publications*, *390*(1), 9–43. https://doi.org/10.1144/SP390.25

French, B. M., Cordua, W. S., & Plescia, J. B. (2004). The rock elm meteorite impact structure, Wisconsin: Geology and shock-metamorphic effects in quartz. *Bulletin of the Geological Society of America*, *116*(1), 200–218. https://doi.org/10.1130/B25207.1

French, B. M., & Koeberl, C. (2010). The convincing identification of terrestrial meteorite impact structures: What works, what doesn't, and why. *Earth-Science Reviews*, *98*(1–2), 123–170. https://doi.org/10.1016/j.earscirev.2009.10.009

Glodny, J., Kühn, A., & Austrheim, H. (2008). Geochronology of fluid-induced eclogite and amphibolite facies metamorphic reactions in subduction-collision system, Bergen Arcs, Norway. *Contributions to Mineralogy and Petrology*, *156*(1), 27–48. https://doi.org/10.1007/s00410-007-0272-y

Griffith, W. A., Rosakis, A., Pollard, D. D., & Ko, C. W. (2009). Dynamic rupture experiments elucidate tensile cracks development during propagating earthquake ruptures. *Geology*, *37*(9), 795–798. https://doi.org/10.1130/G30064A.1

Hielscher, R., & Schaeben, H. (2008). A novel pole figure inversion method: Specification of the MTEX algorithm. *Journal of Applied Crystallography*, *41*(6), 1024–1037. https://doi.org/10.1107/S0021889808030112

Holland, T. J. B., & Powell, R. (1998). An internally consistent thermodynamic data set for phases of petrological interest. *Journal of Metamorphic Geology*, *16*(3), 309–343. https://doi.org/10.1111/j.1525-1314.1998.00140.x

Huffman, A. R., Brown, J. M., Carter, N. L., & Reimold, W. (1993). The microstructural response of quartz and feldspar under shock loading at variable temperatures. *Journal of Geophysical Research*, *98*, 22,171–22,197. https://doi.org/10.1029/93JB01425

Jackson, J. A., Austrheim, H., McKenzie, D., & Priestly, K. (2004). Metastability, mechanical strength, and the support of mountain belts. *Geology*, *32*(7), 625–628. https://doi.org/10.1130/G20397.1

Jamtveit, B., Austrheim, H., & Putnis, A. (2016). Disequilibrium metamorphism of stressed lithosphere. *Earth Science Reviews*, *154*, 1–13. https://doi.org/10.1016/j.earscirev.2015.12.002

Jamtveit, B., Ben-Zion, Y., Renard, F., & Austrheim, H. (2018). Earthquake-induced transformation of the lower crust. *Nature*, *556*(7702), 487–491. https://doi.org/10.1038/s41585-018-0045-y

Jamtveit, B., Bucher-Nurminen, K., & Austrheim, H. (1990). Fluid controlled eclogitization of granulites in deep crustal shear zones, Bergen Arcs, western Norway. *Contributions to Mineralogy and Petrology*, *104*(2), 184–193. https://doi.org/10.1007/BF00306442

Jolivet, L., Raimbourd, H., Labrousse, L., Avigad, D., Leroy, Y., Austrheim, H., & Andersen, T. B. (2005). Softening trigerred by eclogitization, the first step toward exhumation during continental subduction. *Earth and Planetary Science Letters*, *237*(3–4), 532–547. https://doi.org/10.1016/j.epsl.2005.06.047

Kruse, R., Stünitz, H., & Kunze, K. (2001). Dynamic recrystallization processes in plagioclase porphyroclasts. *Journal of Structural Geology*, *23*(11), 1781–1802. https://doi.org/10.1016/S0191-8141(01)00030-X

Mainprice, D., Bachmann, F., Hielscher, R., & Schaeben, H. (2014). Descriptive tools for the analysis of texture projects with large datasets using MTEX: Strength, symmetry and components. *Geological Society, London, Special Publications*, *409*(1), 251–271. https://doi.org/10.1144/SP409.8

Marshall, D. B., & McLaren, A. C. (1977). Deformation mechanism in experimentally deformed plagioclase feldspars. *Physics and Chemistry of Minerals*, *1*(4), 351–370. https://doi.org/10.1007/BF00308845

Menegon, L., Pennacchioni, G., Malaspina, N., Harris, K., & Wood, E. (2017). Earthquakes as precursors of ductile shear zones in the dry and strong lower crust. *Geochemistry, Geophysics, Geosystems*, *18*, 4356–4374. https://doi.org/10.1002/2017GC007189

Miranda, E. A., Hirth, G., & John, B. E. (2016). Microstructural evidence for the transition from dislocation creep to dislocation-accommodated grain boundary sliding in naturally deformed plagioclase. *Journal of Structural Geology*, *92*, 30–45. https://doi.org/10.1016/j.jsg.2016.09.002

Mitchell, T. M., Ben-Zion, Y., & Shimamoto, T. (2011). Pulverized fault rocks and damage asymmetry along the Arima-Takatsuki Tectonic Line, Japan. *Earth and Planetary Science Letters*, *308*(3–4), 284–297. https://doi.org/10.1016/j.epsl.2011.04.023

Mukai, H., Austrheim, H., Putnis, C. V., & Putnis, A. (2014). Textural evolution of plagioclase feldspar across a shear zone: Implications for deformation mechanism and rock strength. *Journal of Petrology*, *55*(8), 1457–1477. https://doi.org/10.1093/petrology/egu030

Newton, R. C., Charlu, T. V., & Kleppa, O. J. (1980). Thermochemistry of the high structural state of plagioclases. *Geochimica et Cosmochimica Acta*, *44*(7), 933–941. https://doi.org/10.1016/0016-7037(80)90283-5

Okudaira, T., Shigematsu, N., Harigane, Y., & Yoshida, K. (2016). Grain size reduction due to fracturing and subsequent grain-size-sensitive creep in lower crustal shear zone in the presence of a CO2-bearing fluid. *Journal of Structural Geology*, *95*, 171–187. https://doi.org/10.1016/j.jsg.2016.11.001

Pickersgill, A., Osinski, G., & Flemming, R. (2015). Shock effects in plagioclase feldspar from the Mistastin Lake impact structure, Canada. *Meteoritics and Planetary Science*, *50*(9), 1546–1561. https://doi.org/10.1111/maps.12495

Poelchau, M. H., & Kenkmann, T. (2011). Feather features: A low-shock-pressure indicator in quartz. *Journal of Geophysical Research*, *116*, B02201. https://doi.org/10.1029/2010JB007803

Poirier, M., & Guillope, J. P. (1979). Dynamic recrystallization during creep of single-crystalline halite: An experimental study. *Journal of Geophysical Research*, *84*, 5557–5567. https://doi.org/10.1029/JB080i010p05557

Putnis, A., & Austrheim, H. (2010). Fluid-induced processes: Metasomatism and metamorphism. *Geofluids*, *10*, 254–269. https://doi.org/10.1111/j.1468-8123.2010.00285.x

Rudnick, R., & Fountain, D. (1995). Nature and composition of the continental crust: A lower crustal perspective. *Reviews of Geophysics*, *33*, 267–309. https://doi.org/10.1029/95RG01302

Stünitz, H., Fitz Gerald, J. D., & Tullis, J. (2003). Dislocation generation, slip systems, and dynamic recrystallization in experimentally deformed plagioclase single crystals. *Tectonophysics*, *372*(3–4), 215–233. https://doi.org/10.1016/S0040-1951(03)00241-5

Sullivan, W. A., & Peterman, E. M. (2017). Pulverized granite at the brittle-ductile transition: An example from the Kellyland fault zone, eastern Maine, U.S.A. *Journal of Structural Geology*, *101*, 109–123. https://doi.org/10.1016/j.jsg.2017.07.002

Svahnberg, H., & Piazolo, S. (2010). The initiation of strain localisation in plagioclase-rich rocks: Insights from detailed microstructural analyses. *Journal of Structural Geology*, *32*(10), 1404–1416. https://doi.org/10.1016/j.jsg.2010.06.011

Thompson, J. B., & Hovis, G. L. (1979). Entropy of mixing in sanidine. *American Mineralogist*, *64*, 57–65.

Trepmann, C., Renner, J., & Druiventak, A. (2013). Experimental deformation and recrystallization of olivine-processes and timescales of damage healing during postseismic relaxation at mantle depths. *Solid Earth*, *4*(2), 423–450. https://doi.org/10.5194/se-4-423-2013

Trepmann, C., Stöckhert, B., Dorner, D., Moghadam, R. H., Küster, M., & Röller, K. (2007). Simulating coseismic deformation of quartz in the middle crust and fabric evolution during postseismic stress relaxation—An experimental study. *Tectonophysics*, *442*(1-4), 83–104. https://doi.org/10.1016/j.tecto.2007.05.005

Wain, A., Waters, D., & Austrheim, H. (2001). Metastability of granulites and processes of eclogitisation in the UHP region of western Norway. *Journal of Metamoprhic Geology*, *19*(5), 609–625. https://doi.org/10.1046/j.0263-4929.2001.00333.x

Wayte, G. J., Worden, R. H., Rubie, D. C., & Droop, G. T. R. (1989). A TEM study of disequilibrium plagioclase breakdown at high pressure: The role of infiltrating fluid. *Contributions to Mineralogy and Petrology*, *101*(4), 426–437. https://doi.org/10.1007/BF00372216

White, J. C. (1993). Shock-induced amorphous textures in plagioclase, Manicouagan, Quebec, Canada. *Contributions to Mineralogy and Petrology*, *113*, 524–532. https://doi.org/10.1007/BF00698320

Zaag, P. T., Reimold, W. U., & Hipsley, C. A. (2016). Microcomputed tomography and shock microdeformation studies on shatter cones. *Meteoritics and Planetary Science*, *51*(8), 1435–1459. https://doi.org/10.1111/maps.12673